

# FZG Rig-Based Testing of Flank Load-Carrying Capacity Internal Gears

B.-R. Höhn, K. Stahl, J. Schudy, T. Tobie and B. Zornek

*(Printed with permission of the copyright holder, the American Gear Manufacturers Association, 1001 N. Fairfax Street, Fifth Floor, Alexandria, VA 22314-1587. Statements presented in this paper are those of the author(s) and may not represent the position or opinion of the American Gear Manufacturers Association.)*

## Management Summary

Micropitting, pitting and wear are typical gear failure modes that can occur on the flanks of slowly operated and highly stressed internal gears. However, the calculation methods for the flank load-carrying capacity have mainly been established on the basis of experimental investigations of external gears.

The target of the research project was to verify the application of these calculation models to internal gears. Therefore two identical back-to-back test rigs for internal gears have been designed, constructed and successfully used for gear running tests. These gear test rigs are especially designed for low and medium circumferential speeds and allow the testing of the flank load-carrying capacity of spur and helical internal gears for different pairings of materials at realistic stresses. The three planet gears of the test rig are arranged uniformly across the circumference. Experimental and theoretical investigations regarding the

load distribution across the face width, the contact pattern and the load-sharing between the three planet gears have been conducted.

Furthermore, substantial theoretical investigations of the characteristics of internal gears were performed. Therefore, internal and external spur gears were compared regarding their geometrical and kinematical differences, as well as their impact on the flank load. Based on the results of these theoretical investigations, an extensive test program of load stage tests and speed stage tests of internal gears of different material, different finishing of the flanks and different operating conditions has been performed. The main focus of this test program was on the fatigue failures—micropitting and wear—at low circumferential speeds.

This paper describes the design and functionality of the newly developed test rigs for internal gears and shows basic results of the theoretical studies. It furthermore presents basic examples of experimental test results.

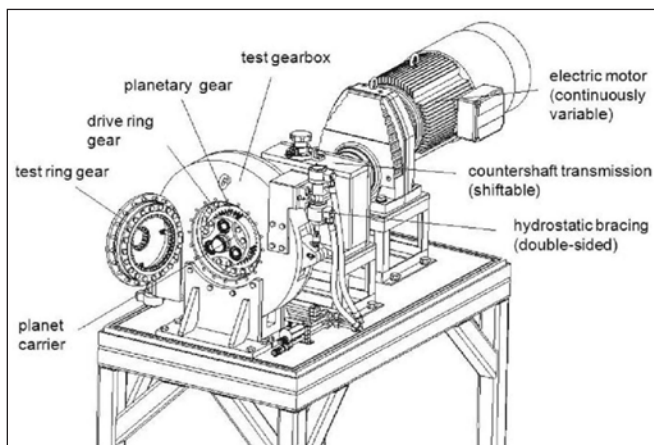


Figure 1—FZG back-to-back test rig for internal gears (schematic representation).

## Introduction

Transmissions for wind turbines and low-speed industrial gear units often feature a slowly operated planetary gear stage. The flanks of these gears can be at risk for micropitting, pitting and wear due to the low circumferential speeds. The increase in power density—especially in transmissions for wind turbine gearboxes—enhances the risk of flank damages.

However, the calculation methods for the flank load-carrying capacity have mainly been established on the basis of experimental investigations of external gears. These calculation methods consider the possible advantages of internal gears regarding geometrical, kinematical and tribological conditions, but in only a limited form. As such, findings of systematic investigations on the flank load-carrying capacity of internal gears are practically nonexistent.

The scope of this research project was to enlarge the state of knowledge on the flank load-carrying capacity of internal gears and to verify the application of the calculation models

to internal gears. Therefore substantial theoretical investigations of the characteristics of internal gears were performed and an extensive program of gear running tests of internal gears was conducted.

### FZG Back-To-Back Test Rig for Internal Gears

In order to carry out the gear running tests on internal gears, two identical, back-to-back test rigs for internal gears were designed and constructed (Fig. 1). These gear test rigs are especially designed for low and medium circumferential speeds and allow the testing of the flank load-carrying capacity of spur and helical internal gears for different pairings of materials at realistic stresses. The essential component of this back-to-back test rig is the test gearbox, in which both test gear and drive gear are situated. The test gear is a planetary gear whose planet carrier is driven by a continuously variable electric motor via a shifttable, countershaft transmission. The three-stepped planet gears of the test rig are arranged uniformly across the circumference and are engaged with the test ring gear as well as the drive ring gear.

By means of the sectional representation of the test gearbox (Fig. 2), the design and functioning of the test rig is explained. The hydrostatic bracing device shown in Figure 1 twists the bracing ring (Fig. 2/2) relative to the two housing parts (Fig. 2/1a and 1b). Spring elements (Fig. 2/3) are used to apply a static torque to the drive ring gear (Fig. 2/4). The spring elements (Fig. 2/3) are mounted uniformly across the circumference and transmit the peripheral forces. They also provide a larger bracing displacement and thereby allow a defined adjustment of the bracing torque. The drive ring gear (Fig. 2/4) can adjust itself freely in radial direction whereby a uniform load-sharing between the three planets (Fig. 2/5) is promoted. The bracing torque is transmitted to the test ring gear (Fig. 2/6) by the planetary gears (Fig. 2/5). The stages of the gearing (Fig. 2/4 and 5; Fig. 2/5 and 6) exhibit the same gear ratio. The symmetrical design of the planetary gears (Fig. 2/5) allows testing of the rear flanks by simply reversing the planets without changing the orientation of bracing. The planets—as well as the planet shafts—are of rigid design so as to reduce irregular load distribution across the face width in the contact between planets (Fig. 2/5) and test ring gear (Fig. 2/6) caused by shaft deflection. The power loss of the test rig is induced via the two-piece planet carrier (Fig. 2/8).

In order to ensure a uniform distribution of the induced torque to the three planetary gears, the drive ring gear (Fig. 2/4) is mounted radially free in the test gearbox. The spring elements (Fig. 2/3) substantially support only peripheral forces. The axial force occurring in helical gears can be supported by thrust washers (Fig. 2/9) mounted in the housing.

Despite the rigidity of the planet gears (Fig. 2/5) and the planet shafts (Fig. 2/7), a slight deflection of these components has to be taken into account. In the same way, a slight torsion of the planet carrier (Fig. 2/8), due to the tilting torque, must also be considered. For this reason an optimization with FEM analysis has been performed.

The torque and rotational speed of the continuously variable electric motor are monitored. Variations in torque and/

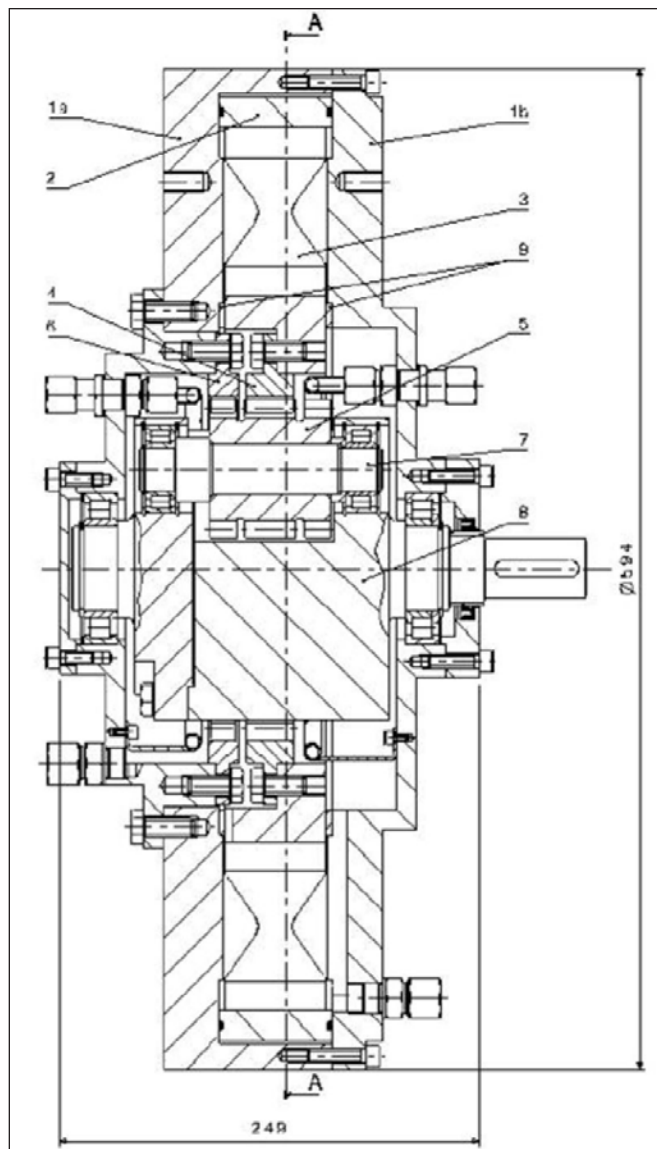


Figure 2—Sectional representation of the test gearbox.

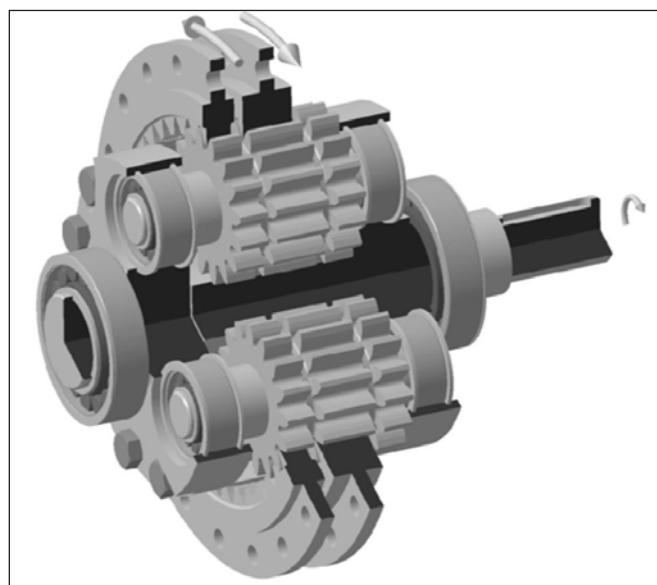
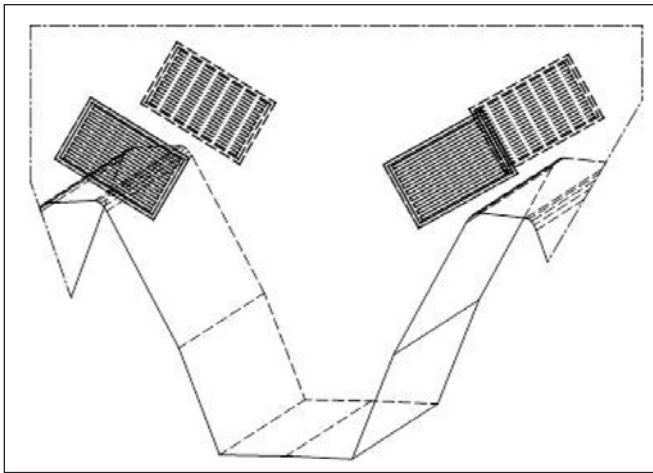


Figure 3—Schematic representation of the assembly of the test gear unit.



**Figure 4—Application of the strain gauges (schematic representation).**

or rotational speed can serve as switch-off criteria. The countershaft transmission (Fig. 1) enables the required low rotational speeds.

The oil feed, with a constant oil temperature, is implemented with oil spray lubrication by an external oil unit. Due to the low rotational speeds, the test and drive gears are wetted around full perimeter by means of annularly arranged spray nozzles.

The two housing parts (Fig. 2/1a and 1b) are screwed together with the grounding to enable application of the bracing torque. The bracing ring (Fig. 2/2) is twisted relative to the housing (Fig. 2/1a and 1b) by two hydraulic cylinders. A strain gage monitoring system was installed to maintain the required constant static bracing torque while operating. The strain gauges are applied to multiple spring elements, arranged uniformly across the circumference.

Table 1 shows the specifications of the FZG back-to-back test rig for internal gears. The range of the circumferential speed from  $v_t = 0.05\text{--}10\text{ m/s}$  allows for the evaluation of micropitting and wear resistance at low speeds, as well as for performing test runs under test conditions comparable to standardized test methods, such as the pitting test ( $v_t = 8.3\text{ m/s}$ ). The dimensioning of the maximum bracing torque was based on the calculative pitting resistance of the pair-

ing of a case-hardened planet with case-hardened ring gear, according to ISO 6336 (Refs. 3 and 4).

The deflection of the planet shafts due to the radial forces resulting from the bracing torque  $T_{rg}$  (Fig. 3), as well as the deformation of planet wheel and planet shaft due to the tilting torque resulting from the double ring gear design, can affect the load distribution across the face width in an unfavorable way. This problem especially occurs in transmissions with stepped planets. An increasing misalignment of the planets results from an increasing bracing torque. A transverse load factor of  $K_{H\beta} = 1.08$  was calculated for the test gear at a bracing torque of  $T_{rg} = 1,500\text{ N}\cdot\text{m}$ , which corresponds to a pitting safety factor of  $S_H \approx 1.0$  for the pairing of a case-hardened planet and a through-hardened ring gear. Considering the twisting of the planet carrier (FEM calculation), a transverse load factor of  $K_{H\beta} = 1.09$  was calculated. However, for a maximum bracing torque of  $T_{rg} = 6,000\text{ N}\cdot\text{m}$ , an even better transverse load factor of  $K_{H\beta} = 1.06$  was calculated (considering the twisting of the planet carrier, also  $K_{H\beta} = 1.06$ ), despite a larger misalignment of the planets. This is due to a more favorable ratio of the maximum-force-per-tooth-width to the average force-per-tooth-width (Eq. 1). (1)

$$K_{H\beta} = \frac{(F/b)_{\max}}{F_m/b}$$

Strain gages have been applied close to the fillet on both sides of the test ring gear in order to analyze the load-sharing between the three planetary gears (Fig. 4). The strain gages have been aligned with the  $60^\circ$  tangents of the fillet because, according to ISO 6336 (Refs. 3 and 4), this is the location of the maximum bending stress for internal gears. The four strain gages are wired in a Wheatstone bridge for temperature compensation. The resulting signal gives information about tooth root bending stress of the test ring gear caused by the three planets. Ideally, the maximum amplitudes of the three signals (planets 1–3) are identical for a constant load. Figure 5 shows the results of the measurements on the load-sharing for different loads at a circumferential speed

**Table 1—Specifications of the FZG back-to-back test rig for internal gears**

Parameter	Unit	Value
rotational speed of the carrier	$n_{\text{carrier}}$	$\text{min}^{-1}$ 5 - 1000
circumferential speed	$v_t$	m/s 0.05 - 10
rated motor torque (power loss)	$T_{\text{motor}}$	Nm 200
maximum bracing torque (test ring gear	$T_{\text{rg,max}}$	Nm 6000

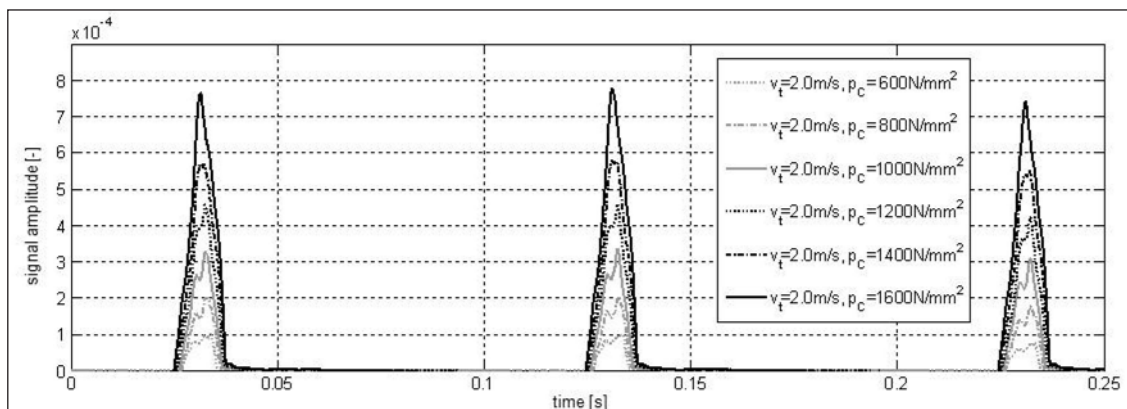


**Figure 5—Measurement of the load sharing between the three planets at  $v_t = 2.0\text{ m/s}$  for different loads.**

of  $v_t=2.0\text{ m/s}$ . The three curves of one load show the signal behavior of the strain gauge measurement during one revolution of the planet carrier, which is proportional to the maximum tooth root bending stress. In this case, the second tooth contact caused a slightly higher bending stress than the two other tooth contacts. However, the measurement indicates good load-sharing behavior between the three planets.

In order to evaluate the contact pattern of the test gears in the FZG back-to-back test rig for internal gears, a contact pattern check with contact pattern paint was performed at a medium load ( $p_c=400\text{ N/mm}^2$ ). The contact pattern paint was removed with relative consistency across the face width of all teeth of the three planets and the ring gear. Therefore, the good load distribution across the face width—as well as the consistent load sharing between the three planets—could be confirmed.

### Theoretical Investigations on the Characteristics of Internal Gears

The theoretical investigations were performed by comparing an external gear to an internal gear. The external gear for these theoretical studies is of the standard FZG test gear type C, which is also used in multiple standard gear running tests like the FZG–FVA pitting test, the FZG–FVA micropitting test and the FZG–DGMK wear test. The pinion of the external gear and the planet of the internal gear have the same tooth geometry. Table 2 summarizes the main gear data of both gears. The internal gear was also used for the gear running tests within the experimental investigations.

For the external gear, the beginning of contact (point A) is in the area of the dedendum flank of the pinion. In contrast, the beginning of contact (point A) for the internal gear was laid in the area of the dedendum flank of the ring gear. These drive directions are consistent with the most common applications in practice. For the external gear this is the configuration with a driving pinion, while internal gears—especially in the application range of wind turbines—are often operated with a reverse-drive direction (driving ring gear).

It should first be noted that external gears are a pairing of convex/convex flanks, whereas internal gears are a pairing of convex/concave flanks. Because of these geometrical conditions, the pinion of the external gear shows an increasing radius of curvature ( $\rho_1$ ) along the transverse path of contact (AE), while the radius of curvature of the wheel ( $\rho_2$ ) is decreasing (Fig. 6). This leads to an equivalent radius of curvature ( $\rho_{eq}$ ) that can be regarded as being nearly constant in comparison to the internal gear. The absolute values of

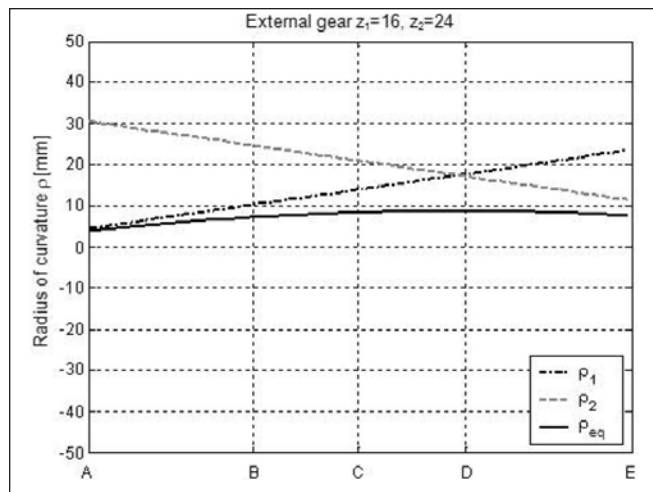


Figure 6—Radius of curvature of the external gear (beginning of contact: dedendum flank of the pinion).

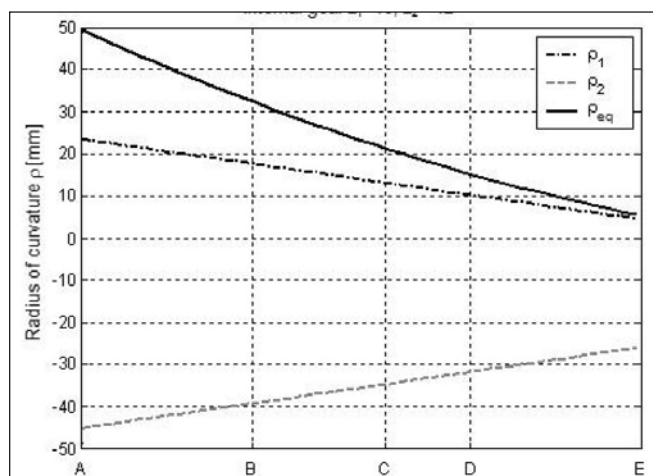


Figure 7—Radius of curvature of the internal gear (beginning of contact: dedendum flank of the ring gear).

Table 2—Gear data of external and internal gear for the theoretical studies

Parameter	Unit	External gear		Internal gear	
		Pinion	Wheel	Planet	Ring gear
normal module $m_n$	mm	4.5			
number of teeth $z$		16	24	16	-42
face width $b$	mm	14.0			
pressure angle $\alpha_n$	°	20.0			
helix angle $\beta$	°	0			
addendum modification coefficient $x$	—	0.1817	0.1715	0.1817	-0.2962
tip circle diameter $d_a$	mm	82.5	118.4	82.5	-185.0
center distance $a$	mm	91.5		-59.0	

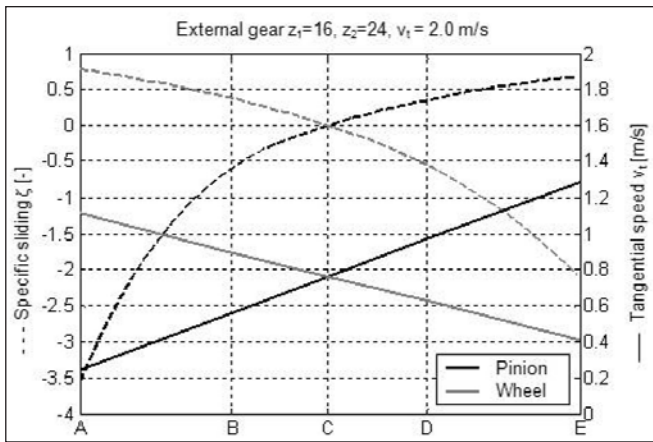


Figure 8—Specific sliding and tangential speed of the external gear.

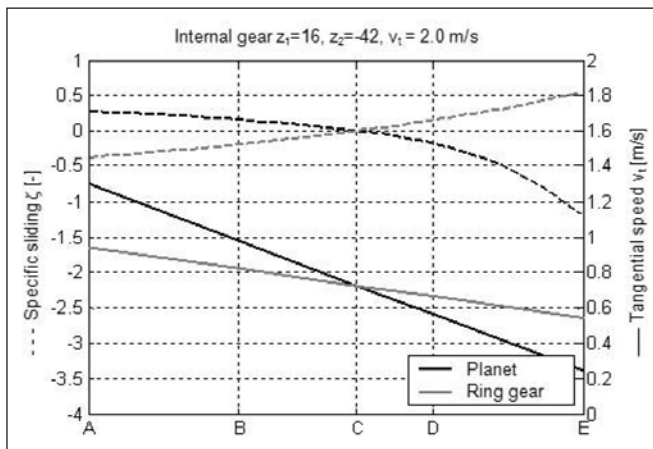


Figure 9—Specific sliding and tangential speed of the internal gear.

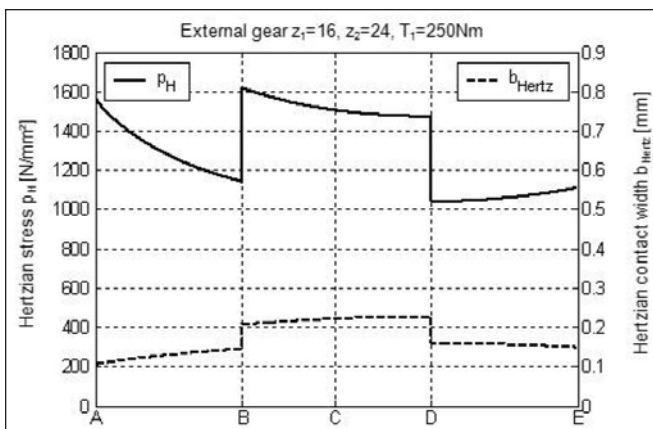


Figure 10—Hertzian pressure and Hertzian contact width of the external gear.

the radiuses of curvature of planet ( $\rho_1$ ) and ring gear ( $\rho_2$ ) of the internal gear, both starting at high values, are decreasing along the transverse path of contact (Fig. 7). This leads to a high equivalent radius of curvature ( $\rho_{eq}$ ) in the beginning of contact, which continuously decreases over AE. The equivalent radius of curvature in point A of the external gear is comparable to the equivalent radius of curvature in the equivalent point E of the internal gear.

Figures 8 and 9 show that negative, specific sliding occurs in the area of the dedendum flank of pinion and wheel of the external gear, as well as in the planet and ring gear of the internal gear. Compared to the external gear, the absolute values of the specific sliding for the internal gear are significantly lower. However, for the internal gear, the negative, specific sliding of the planet is more distinct than the negative, specific sliding of the ring gear.

The mean sum of velocity for both gears can be calculated by adding the tangential speeds of the two engaged gearwheels. Figure 8 shows that the tangential speed of the driving gear of the external gear increases over the transverse path of contact (AE), while the tangential speed of the driven gear decreases equally; therefore the mean sum of velocity stays approximately constant. In contrast, the tangential speeds of both gearwheels of the internal gear (Fig. 9) start at their maximum values in the beginning of contact, and both decrease over AE—which leads to a decreasing sum of velocity. This results in an improvement of the hydrodynamic conditions in the beginning of contact which, in combination with the favorable equivalent radius of curvature, suggests that the area of the dedendum flank of the ring gear is exposed to a smaller risk of failure than the equivalent area of the wheel of the external gear. The tangential speeds shown in Figures 8 and 9 relate to a circumferential speed of  $v_t=2$  m/s.

Figures 10 and 11 show the Hertzian contact pressure  $p_H$  and the Hertzian contact width  $b_H$  over the respective transverse path of contact for an identical torque ( $T_1=250$  N-m) on the pinion of the external gear and the planet of the internal gear. This load corresponds to the common fatigue strength of a case-hardened type C gear. The Hertzian pressure in the area of the dedendum flank of the ring gear of the internal gear is, compared to the wheel of the external gear, significantly lower. As a result, favorable conditions exist with regard to the flank load-carrying capacity this area. The area of the dedendum flank of the planet—at risk of micropitting due to negative specific sliding—is subjected to higher loads than the respective area of the ring gear due to the smaller equivalent radius of curvature.

Figures 12 and 13 show the calculated flash temperatures along the transverse path of contact—according to Blok (Ref. 10)—for the given torque and a surface roughness of  $R_a=0.3$   $\mu$ m. The flash temperature serves as a measure of the contact temperature in the tooth contact and is presented for the reference lubricant FVA 3 + 4% Anglamol 99, and a range of circumferential speed from  $v_t=2.0-0.05$  m/s in both diagrams. It shows that the flash temperatures for the internal gear are significantly lower than for the external gear over the complete path of contact—with exception of the pitch

point C. These lower contact temperatures, in essence, imply a tribological advantage over the external gear regarding risk of scuffing—especially at higher circumferential speeds.

The relative thickness of the lubricating film  $l$ , considering the flash temperature, for external and internal gear, is shown in Figures 14 and 15. The calculated values of the thickness of the lubricating film also relate to the reference lubricant FVA 3+4 % Anglamol 99 (ISO VG 100) at an injection temperature of 60°C. The more favorable hydrodynamic conditions at the beginning of contact of the internal gear are also apparent in the run of the thickness of the lubricating film. Yet, at the end of the transverse path of contact (point E), the internal gear shows low thicknesses of the lubricating film comparable to the conditions in the beginning of contact (point A) of the external gear.

If one examines both external and internal gear with regard to the threat of micropitting, the ring gear of the internal gear has the advantage that the Hertzian contact pressure in the area of negative, specific sliding is low due to the high values of the radius of curvature. This suggests, assuming equal material and heat treatment of the gears, that the area of the dedendum flank of the ring gear is exposed to significantly lower risk of micropitting than the equivalent area of the wheel of the external gear. Negative, specific sliding also occurs in the area of the dedendum flank of the planet. In contrast to the area of the dedendum flank of the ring gear, this area is exposed to the maximum value of the Hertzian pressure (Fig. 11) and the minimum value of the thickness of the lubricating film (Fig. 15). As a result, it is assumed that on internal gears micropitting predominantly occurs in the area of the dedendum flank of the planet.

### Experimental Test Results

Within an extended research project (Refs. 8 and 9), an extensive test program has been conducted in the FZG back-to-back test rig for internal gears. The main focus of this test program was the gear failure modes micropitting and wear; it therefore covered numerous load stage and speed stage tests on internal gears of different material, different finishing of the flanks and different operating conditions. The reference operating conditions for the experimental tests are summarized in Table 3.

The load stage tests have all been performed at a constant circumferential speed of  $v_t=2.0$  m/s (Table 4). According to the standard micropitting test (Ref. 2), the duration of the load stages was set to 16 h/stage. The Hertzian pressure is gradually raised between two stages. Thereby, the load stage test allows comparison of information regarding the load impact on the pitting, micropitting and wear behavior of the analyzed variants. For the material pairing of the case-hardened planet and through-hardened ring gear, load stages 1–6 were performed. For the material pairing of the case-hardened planet and case-hardened ring gear, the load was consecutively increased from load stage 6 to load stage 11.

In the speed stage test, in contrast to the load stage test, the circumferential speed is varied while the load is held constant. The load for the speed stage tests was chosen in such a way that pitting was unlikely to occur (load stage 4 for the

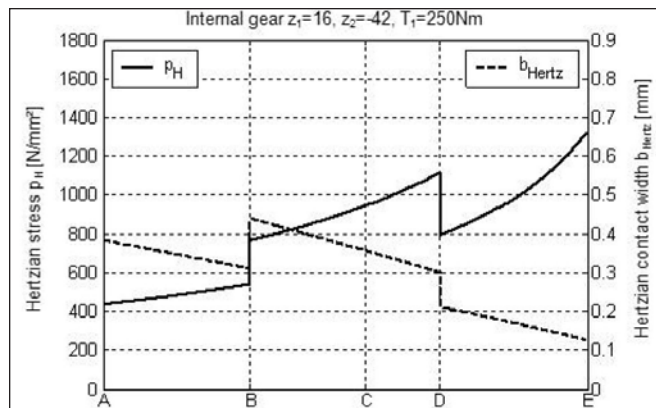


Figure 11—Hertzian pressure and Hertzian contact width of the internal gear.

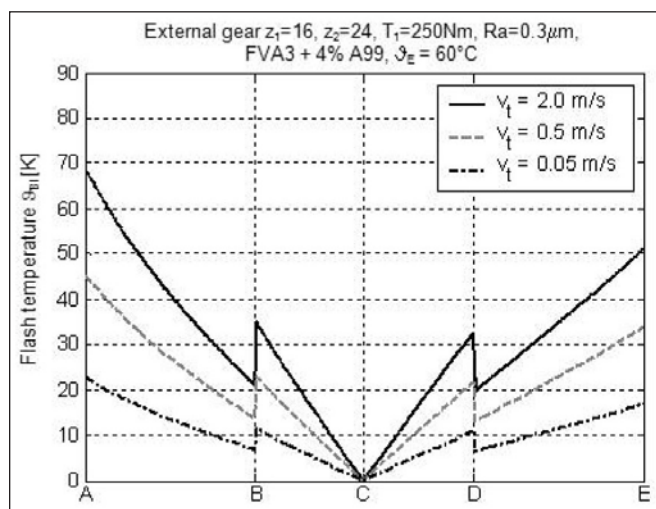


Figure 12—Flash temperature as a measurement of the contact temperature of the external gear.

Table 3—Reference operating conditions for the experimental test on internal gears

Parameter	Unit	Value
lubrication type		oil spray lubrication
injection volume	l/min	2
injection temperature	°C	60
reference lubricant		FVA 3+4% Anglamol 99
reference driving direction		driving ring gear

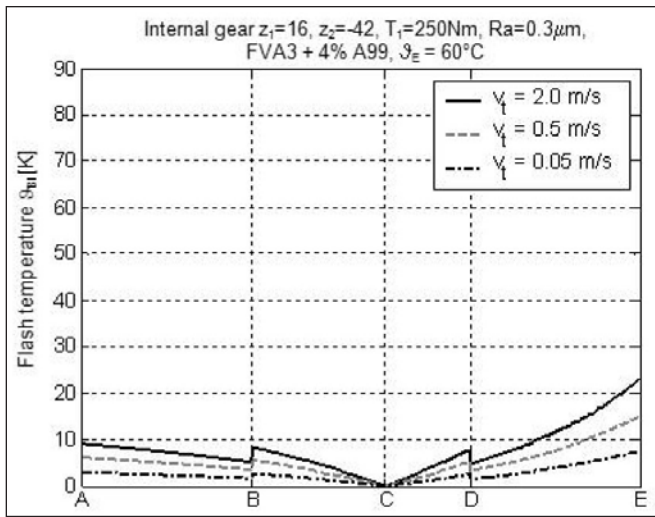


Figure 13—Flash temperature as a measurement of the contact temperature of the internal gear.

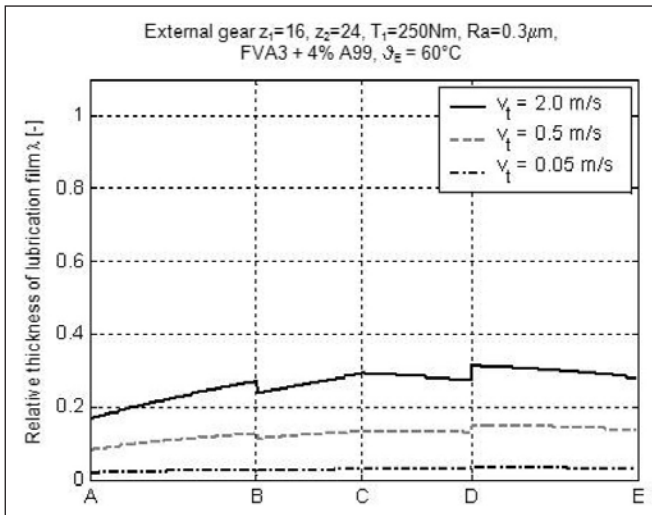


Figure 14—Relative thickness of the lubricating film for the external gear.

pairing of case hardened/through hardened; load stage 11 for the pairing of case-hardened/case-hardened). The duration of the speed stages was also set to 16 h/stage. Because of the number of planets and a gear ratio of  $z_2/z_1 = 2.625$ , the load-cycles-per-unit-of-time are reasonably comparable.

The extensive program of gear running tests showed that the calculation of the micropitting resistance according to FVA 259/I (Refs. 1 and 7), as well as the calculation of the wear resistance according to FVA10 (Refs. 5 and 6), can be directly applied to internal gears. Furthermore the test results basically support calculation of the pitting resistance according to ISO 6336 (Refs. 3 and 4). The following sections briefly summarize a few results of the experimental investigations.

Within the performed research project, the pitting resistance was not examined systematically. However, fundamental statements for the pairing of the case-hardened planet (18CrNiMo7-6) with a through-hardened ring gear (42CrMo4) can be made based on the results of the load stage tests. The first, smaller pitting areas for this material pairing were monitored after load stage 5 ( $p_C = 700 \text{ N/mm}^2$ ). The load stage test was stopped after load stage 6 ( $p_C = 800 \text{ N/mm}^2$ ) because progressive pitting was observable. Following the load stage test, an endurance test at the same load ( $p_C = 800 \text{ N/mm}^2$ ) was performed, since no failure criteria regarding the pitting area had yet been developed. Figure 16 shows one tooth flank of the through-hardened ring gear after the endurance test (3 million load cycles on the ring gear). The conversion of the Hertzian pressure  $p_C$  according to ISO 6336 (Refs. 3 and 4), resulted in a contact stress of  $\sigma_H = 750 \text{ N/mm}^2$ , which is slightly higher than the common, permissible contact stress for this material ( $\sigma_{Hlim} = 700 \text{ N/mm}^2$ ; 42CrMo4V). Therefore it is possible to classify the result of the endurance test according to the current state of knowledge. In addition, Figure 16 shows that pitting on ring gears typically occurs in the area of singular contact and negative, specific sliding (points B and C). In contrast to external gears, the maximum stress in the area of the dedendum flank of the ring gear occurs directly at the pitch point C. It was observed that pitting particularly progressed in the area of the pitch point. As a result, ISO 6336 consequentially determines the contact stress  $\sigma_H$  at the pitch point.

Table 4—Load stages for the internal gear (load stage test)

Load stage	Hertzian pressure, $\text{N/mm}^2$	Duration per stage, h	Torque, Nm	
			$T_1$ (planet)	$T_2$ (ring gear)
1	300	16	25.2	198.3
2	400		44.8	352.8
3	500		70.0	551.1
4	600		100.8	793.8
5	700		137.2	1080.3
6	800		179.2	1411.2
7	950		255.4	2010.9
8	1100		338.8	2667.9
9	1250		437.5	3445.2
10	1400		548.8	4321.8
11	1550		672.6	5297.1

The micropitting and wear resistance of the paired case-hardened planet and case-hardened ring gear (18CrNiMo7-6) were examined in numerous speed stage tests. The speed stage tests for this material pairing were performed at a Hertzian contact pressure of  $p_c = 1,550 \text{ N/mm}^2$ . With decreasing circumferential speed in the speed stage tests, a change of failure modes was monitored. The results showed an overlapping of failure modes micropitting and wear. Figure 17 shows pictures of one tooth flank of a case-hardened planet after the different stages of the speed stage test. The case-hardened planet already displayed initial micropitting in the area of the dedendum flank after the first stage, with a circumferential speed of  $v_t = 2.0 \text{ m/s}$ . This micropitting area moderately increased until speed stage 5 ( $v_t = 0.25 \text{ m/s}$ ). During speed stage 6, enhanced wear-related changes of the tooth surface were monitored; the micropitting area was removed due to abrasive wear.

The corresponding ring gears did not show any damage or noteworthy changes of the surface structure in speed stages 1–5 ( $v_t \geq 0.25 \text{ m/s}$ ). However, for lower circumferential speeds ( $v_t < 0.25 \text{ m/s}$ ), significant wear-related damage of the tooth flanks was monitored (Fig. 18).

These results show that, in the respective range of circumferential speeds, only the planets are exposed to risk of micropitting. Given that micropitting typically occurs in the area of negative, specific sliding, these test results are in agreement with the results of theoretical studies that have shown that the area of the dedendum flank of the planet is subject to negative, specific sliding and high Hertzian pressure, while the dedendum flank of the ring gear—also subject to negative, specific sliding—is exposed to considerably lower values of Hertzian pressure. In contrast, the tooth flanks of both planet and ring gear can show wear-related damage for low circumferential speeds. The involute profiles at the end of the speed stage test (Figs. 19 and 20) show that the changes of the profile of the planet due to micropitting and abrasive wear are more distinct than the changes of the profile of the ring gear. For both planet and ring gear, the

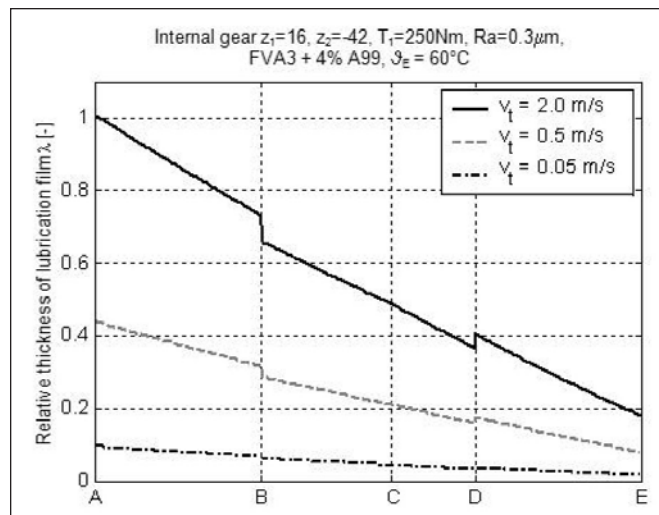


Figure 15—Relative thickness of the lubricating film for the internal gear.

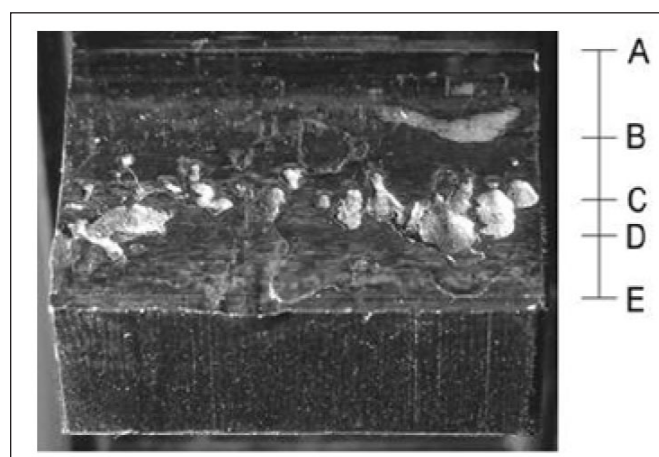


Figure 16—Pitting on the tooth flank of a through-hardened ring gear ( $p_c = 800 \text{ N/mm}^2$ ).

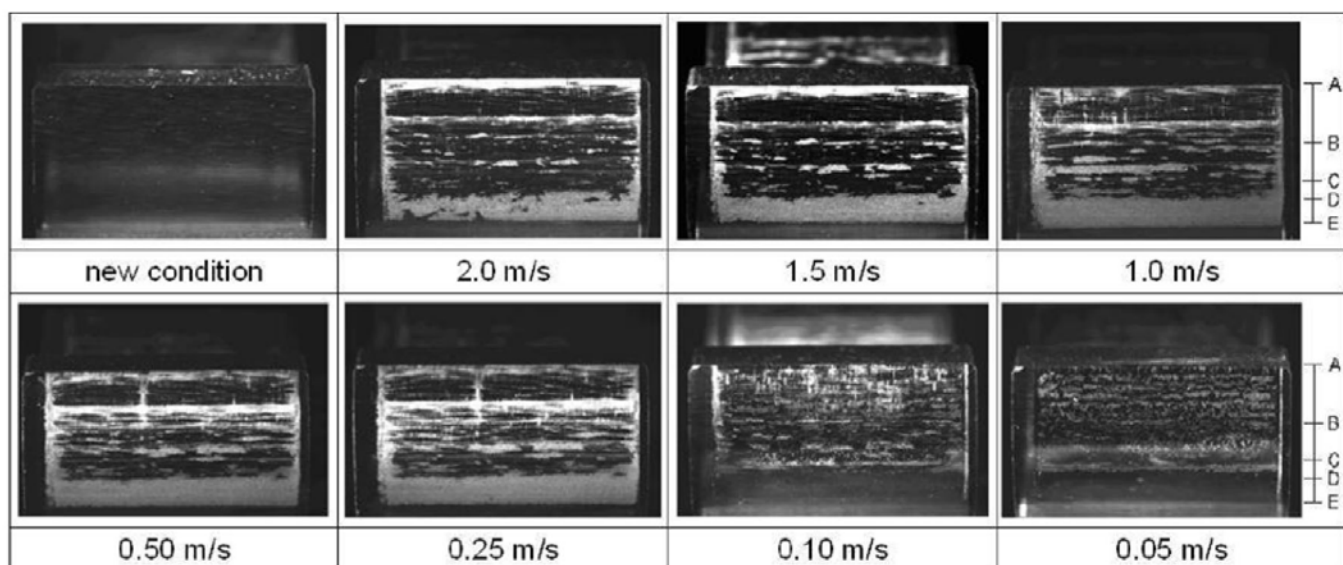


Figure 17—Exemplary pictures of one tooth flank of a case hardened planet in new condition and after every stage of the speed stage test;  $R_a = 0.3 \mu\text{m}$ .

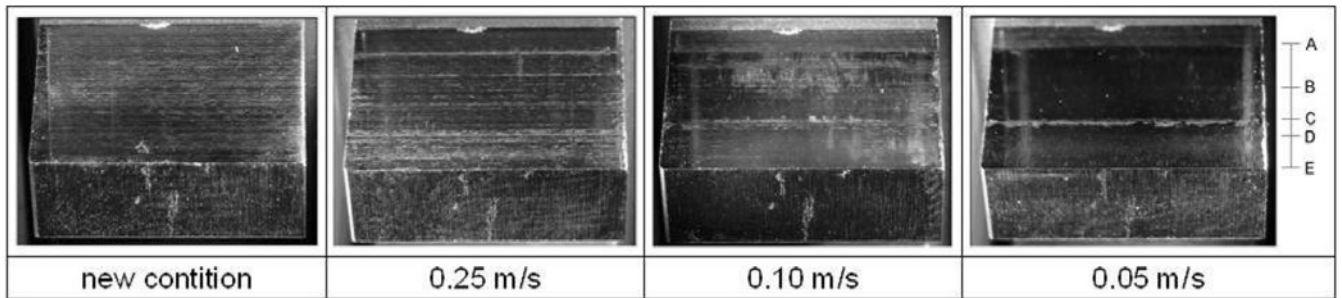


Figure 18—Exemplary pictures of one tooth flank of a case-hardened ring gear in new condition and after the relevant stages of the speed stage test ( $v_t \leq 0.25$  m/s;  $R_a = 0.3$   $\mu\text{m}$ ).

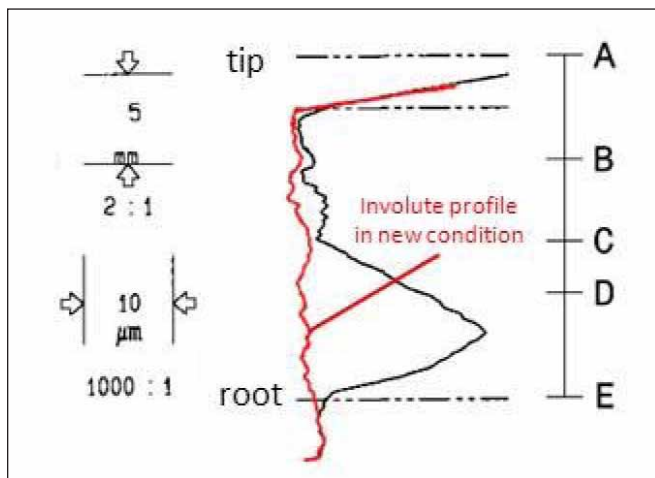


Figure 19—Involute profile of the tooth of a planet in new condition and after the end of the speed stage test.

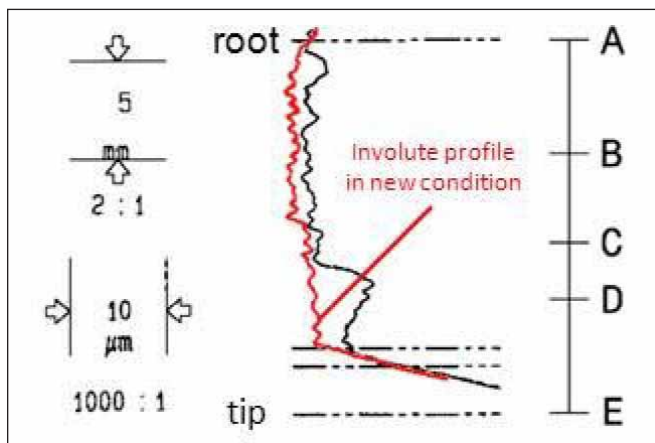


Figure 20—Involute profile of the tooth of a ring gear in new condition and after the end of the speed stage test.

location of maximum damage is in the area of maximum contact stress due to minimal, equivalent radius of curvature. Thus, the planet shows maximum changes of the involute profile in the area of the dedendum flank, while the ring gear shows maximum damage in the area of the addendum flank.

### Summary

Pitting, micropitting and wear are typical gear failure modes that can occur on the flanks of slowly operated and highly stressed internal gears. In order to verify the calculation methods for the flank load-carrying capacity, substantial theoretical studies, as well as an extensive program of gear running tests, have been conducted. Therefore, two identical back-to-back test rigs for internal gears have been designed, constructed and successfully used for experimental tests.

Theoretical studies have shown that the area of the dedendum flank ring gear—which is at risk of micropitting and pitting due to negative, specific sliding—benefits from a high equivalent radius of curvature and low values of the specific sliding. This results in relatively low contact stress and relatively thick lubricating film. In contrast, the area of the dedendum flank of the planet is exposed to considerably higher values of the specific sliding and Hertzian pressure, while the relative thickness of the lubricating film is significantly lower. With that stipulation—assuming comparable material and heat treatment—pitting and micropitting will almost exclusively occur on the flanks of the planet of the internal gear.

The experimental tests have shown that calculation of the micropitting (Refs. 1 and 7) and wear resistance (Refs. 5 and 6) can be applied to internal gears. The procedure of the calculation of the pitting resistance (Refs. 3 and 4) was also supported by test results. Furthermore, the gear running tests have shown that an existing micropitting area, which had been generated at medium circumferential speeds ( $v_t = 0.25$  m/s), can be overlapped and removed by wear-related damage of the flank at low circumferential speeds ( $v_t < 0.25$  m/s).

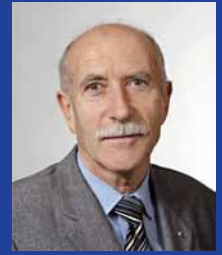
Further results of the experimental investigations are given in References 8 and 9.

*Acknowledgement. This research project was sponsored by the working group of Industrieller Research Associations Registered Association (AiF) with funds from the Federal Ministry for Economics (BMWi) and the Research Association for Propulsion Technology (FVA).*

## References

1. FVA paper No. 259/2. "Grey Mark Load-Carrying Capacity: Practical Revision Against Grey Spottiness; Estimation of a Grey Mark Endangerment or Grey-Mark-Safety; Necessary Grey Mark Load-Carrying Capacity; Lubricant Estimation of One Transmission Lifespan; Regarding Scouring by Grey-Spottiness-Local Computation of the Scouring," Frankfurt, 1999.
2. FVA Paper No.54/7. "Grey Mark Test C/8.3/90: Research Association Propulsion Technology," Frankfurt, 1993.
3. ISO 6336-1:2006. Calculation of Load-Capacity of Spur and Helical Gears, Part 1: Basic Principles—Introduction and General Influence Factors.
4. ISO 6336-2:2006. Calculation of Load Capacity of Spur and Helical Gears, Part 2: Calculation of Surface Durability (Pitting).
5. Plewe, H.-J. "Influence of Lubricant and Material on the Wear of Slowly Running Gear Wheels (Peripheral Speeds Under 0.2 m/s)," FVA Research Project No. 10/I, FVA Booklet No. 30, Frankfurt, 1976.
6. Plewe, H.-J. "Influence of Lubricant, Material and Load on the Wear of Slow-Current Gear Wheels (Peripheral Speeds under 0.5 m/s)," FVA Research Project No. 10/II, FVA Booklet No. 79, Frankfurt, 1979.
7. Schrade, U. "Influence of Tothing Geometry and Operating Conditions on Grey Mark Load-Carrying Capacity of Gears," FVA Research Project 259/I, FVA Booklet No. 583, Frankfurt, 1999.
8. Schudy, J. "Flank Strength of Interior and Outer Spline Spur Wheels with Small Peripheral Speeds," FVA Research Project No. 482, FVA Booklet No. 867, Frankfurt, 2008.
9. Schudy, J. "Investigation of the Flank Strength of Outside and Internal Teeth," Thesis, TU München, 2010.
10. Theyse, F.-H. "The Lightning Temperature Method After Blok and Its Practical Application with Gear Wheels," *Lubrication Technology* 1, 1967.

**Dr.-Ing. Bernd-Robert Höhn** studied mechanical engineering at the Technical University Darmstadt (1965–1970) and served as an assistant lecturer (1970–1973) at the Institute for Machine Elements and Gears at the Technical University Darmstadt prior to becoming an assistant professor at the university (1973–1979); in 1978, he received his PhD (Dr. Ing.) in mechanical engineering. In early April, 1979 Höhn worked as a technical designer in the department for gear development of the Audi, and by 1982 was head of the department for gear research and design for the automaker. In 1986 Audi named Höhn department head for both gear research and testing of automotive transmissions, until his departure in 1989 to become head of both the Institute of Machine Elements at the Technical University and of the Gear Research Centre (FZG). Since 2011, he has served as director emeritus of the Institute. Höhn has also served as vice president for VDI for research and development, as well as leader of working groups 6 and 15 for ISO TC 60—calculation of gears.



**Prof. Dr.-Ing. Karsten Stahl** became head of the Institute for Machine Elements and the Gear Research Centre (FZG) at the Technical University of Munich in 2011. As the successor to Dr. Höhn, Stahl directs more than 60 employees at the institute, which focuses on examination and testing of machine elements, such as gears, bearings, synchronizations and couplings.



**Dr.-Ing. Thomas Tobie** is a department leader at the Institute for Machine Elements – Gear Research Centre (FZG). His research specialties are in the fields of heat treating, gear material and gear load capacity regarding tooth root bending fatigue, pitting and micropitting.



**Juergen Schudy** is a research associate at the Institute for Machine Elements – Gear Research Centre (FZG).

**Dipl.-Ing. Bernd Zornek** is a research associate at the Institute for Machine Elements – Gear Research Centre (FZG).

